# Average Heat Flux Measurements in a Gaseous Detonation-Based Rocket Engine

Matthew A. Maybee*, Micheala Hemming*, Kaito J. Durkee*, Justin Byers*
*University of Alabama in Huntsville, Huntsville, Alabama, 35899, USA*

Joseph Hernandez-McCloskey†
*The University of Texas at San Antonio, San Antonio, TX, 78249, USA*

Kunning G. Xu‡, John W. Bennewitz§
*University of Alabama in Huntsville, Huntsville, Alabama, 35899, USA*

Thomas Teasley¶
*NASA Marshall Space Flight Center, Huntsville, AL, 35808, USA*

**Rotating detonation rocket engines (RDREs) offer benefits over traditional deflagrative engines, including increased engine performance, compact combustion and negligible detrimental thermoacoustic instabilities due to mode-locking. Realizing the benefits of a detonation-based propulsion system will be accompanied by increased thermal loads due to a combination of heat release at elevated pressure and temperature, as well as compact heat release due to detonation. Managing these heat loads necessitates the development of thermal management strategies. As a first step towards establishing the requirements for detonation-based engine thermal management strategies, this work develops an additively manufactured (AM) water-based, axially resolved calorimeter for integration in an existing 76.8 mm outer diameter (OD) RDRE to measure average chamber heat flux. In particular, the calorimetry outer body provides average heat flux data via circumferential channels at nine axial stations to axially resolve the heat flux distribution on the chamber outer wall. The average heat flux is found to be 5 – 12 MW/m$^2$ for a straight annulus and 6 – 18 MW/m$^2$ for a constricted annular configuration which exhibited maximum heat flux at the throat. A difference in heat flux scaling is observed near the detonation region compared to the downstream flow expansion section in the constricted geometry. By quantifying the axial distribution of heat flux, this work seeks to support the development of thermal management systems for long duration firing of detonation-based devices.**

## I. Nomenclature

| | | |
|---|---|---|
| $\phi$ | = | equivalence ratio |
| $\psi$ | = | total mass flux, kg/m$^2$-s |
| $A$ | = | cross-sectional area, m$^2$ |
| $A_{\text{hot}}$ | = | coolant channel hot side area, m$^2$ |
| $A_{\text{side}}$ | = | coolant channel side wall area, m$^2$ |
| $A_{\text{cool}}$ | = | coolant channel cross-sectional area, m$^2$ |
| $A_{\text{outer}}$ | = | combustor outer wall area, m$^2$ |
| $C_{\text{p}}$ | = | specific heat at constant pressure, kJ/kmol-K |
| $\bar{c}$ | = | average specific heat at constant pressure, kJ/kmol-K |
| $D_{\text{h}}$ | = | hydraulic diameter, m |
| $t_{\text{wall}}$ | = | channel wall thickness, m |

*Graduate Research Assistant, Department of Mechanical and Aerospace Engineering, AIAA Student Member
†Graduate Research Assistant, Department of Mechanical Engineering, AIAA Student Member.
‡Professor, Department of Mechanical and Aerospace Engineering, AIAA Associate Fellow.
§Assistant Professor, Department of Mechanical and Aerospace Engineering, AIAA Senior Member
¶Combustion Devices Engineer, Engine Component Development and Technology Branch, AIAA Member

$\dot{m}$ = mass flow rate, kg/s
$T_{out}$ = outlet temperature, K
$T_{in}$ = inlet temperature, K
$T_{bulk}$ = coolant bulk temperature, K
$T_{wall}$ = cooling channel hot wall temperature, K
$p$ = pressure, MPa
$\dot{q}$ = heat transfer rate, MW
$\dot{q}_{tot}$ = total heat transfer rate, MW
$\dot{q}_{h}$ = cooling channel hot wall heat transfer rate, MW
$\dot{q}$" = heat flux, MW/m$^2$
$v_{cool}$ = coolant velocity, m/s
$\rho$ = coolant density, kg/m$^3$
$\mu$ = coolant dynamic viscosity, N-s/m$^2$
$\kappa$ = thermal conductivity, W/m-K
$C_d$ = discharge coefficient
$\epsilon_c$ = contraction ratio
$t_b$ = burn time, s
$m$ = wave number
$h_c$ = liquid film heat transfer coefficient, W/m$^2$-K
$h_{c,req}$ = required heat transfer coefficient, W/m$^2$-K
$\beta$ = ratio of diameters
$d$ = distance between cooling channels, m

## II. Introduction

ROTATING detonation rocket engines (RDREs) have garnered recent interest due to various benefits including compact combustion and increased theoretical performance compared to deflagrative engines. These devices implement detonation as the primary means of combustion to generate heat release at high temperatures and pressures allowing for more useful work to be extracted [1]. However, this increased heat release poses an engineering challenge requiring further investigation to fully realize these benefits.

Currently, a majority of RDRE experimental work incorporates heat-sink geometries for short duration fires to avoid damage caused by these increased heat loads [2, 3]. One heat-sink hardware study performed measurements of wall heat flux for a 76.2 mm OD in Micka et al. [4], finding the maximum heat flux in the detonation region near the injector to be 23.6 MW/m$^2$. Additionally, heat flux near the injection plane did not follow the traditional mass flux scaling of the Bartz correlation for equivalent deflagrative devices [4, 5]. High-frequency heat flux measurements taken by Theuerkauf et al. [6, 7] show heat flux ranging from $1 - 9$ MW/m$^2$ for a 152.4 mm water-cooled RDRE. Additively manufactured actively-cooled chambers have also been explored using axial channels to enable long duration testing and calorimetry measurements of detonation-based rocket engines [8, 9]. However, circumferential channels offer the ability to reveal the axial heat flux distribution over the length of the combustor. This approach is implemented by Aliakbara et al. [10] who demonstrated axially resolved water-based calorimetry measurements of a 100 mm mean diameter combustor. Location and magnitude of maximum heat flux is shown to be dependent upon injector design, with the maximum measured heat flux around $8 - 9$ MW/m$^2$ [10].

The associated heat loads of RDREs necessitate the development of thermal management systems to enable their implementation in practical propulsive systems such as launch, boost, and lander systems [11]. Actively-cooled hardware requires the manufacturing of complex cooling channel geometries, which is made easier by additive manufacturing when compared to traditional subtractive methods. Recent improvements in AM are leveraged to produce the complex geometries necessary for axially resolved actively-cooled calorimetry hardware. AM geometries provide a path forward to more rapidly increase the technological readines level of RDREs by enabling increased test durations, as well as provide means to collect average heat flux measurements.

The present work develops an axially resolved, additively manufactured 76.8 mm OD calorimeter using gaseous methane ($GCH_4$) and oxygen ($GO_2$) as propellants, which serves as a first step to establishing the heat flux levels in different scale detonation-based engines. Average heat flux measurements are taken with a water-based calorimeter at nine axial stations to more completely resolve the heat flux experienced by the RDRE chamber. Heat flux obtained in the present work increases the understanding of the heat flux loadings experienced within RDREs, and aids in the

development of thermal management strategies enabling long duration operation of detonation-based rocket propulsion systems.

## III. Hardware

### A. Heat-Sink Hardware

In the current work, a water-based outer body calorimeter is designed to enable long duration burn times through the implementation of sufficient cooling to the combustor wall while providing finely resolved axial heat flux measurements. The RDRE tested is an AM 76.8 mm OD RDRE that implements a modular design consisting of (1) an outer body, (2) an inner body, (3) an expanding nozzle, and (4) an injector manifold (see Fig. 1). As the hardware is modular, it can be tested with various configurations of different injector, outer body, and inner body designs.

For the present work, a straight heat-sink outer body and a water-cooled calorimetry outer body are tested. Additionally, two center body designs are evaluated: a straight center body and a constricted center body with a contraction ratio of $\epsilon_c = 2.34$ where the throat is located at $x/L = 0.77$ (Fig. 2(b)). The contraction ratio required to achieve a desired chamber pressure is determined using an in-house RDRE thermodynamic model [12], based on the work of Burr and Paulson [13]. The straight center body has a diameter of 63.5 mm and an annular width of 6.65 mm. The expansion ratio of the nozzle is 5.1 when using the straight center body and 12.7 with the constricted center body. For the straight center body configuration, the outer-diameter-to-length-ratio is unity while it is 0.77 when implementing the constricted center body. Due to area constraints, neither of the center body designs are actively-cooled. The center body is secured with a bolt that passes through the injector manifold and threads into the 30° conical tip of the center body. During testing, a silicone o-ring is used to protect the bolt from hot combustion gases. The injector manifold consists of the oxidizer and fuel manifolds that supply uniform propellant flow to a standard impingement injector. The components of the hardware are held together by four bolts passing through the expansion nozzle and injector manifold.

For this study, the RDRE hardware is tested in three different configurations: (1) heat-sink straight channel (Fig. 1(a)), (2) water-cooled straight channel (Fig. 1(b)), and (3) water-cooled constricted geometry (see Fig. 1(c)). The heat-sink straight channel configuration consists of the straight center body and the straight heat-sink outer body, while the water-cooled straight channel and constricted geometry configurations utilize the water-cooled calorimetry outer body with the straight and constricted center bodies, respectively.

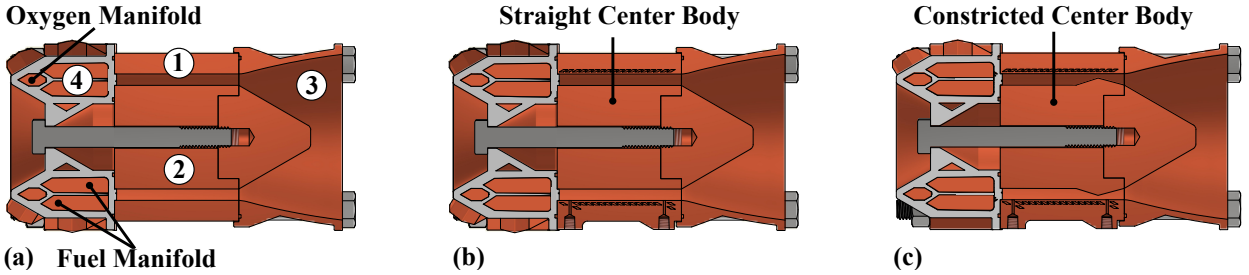



**Fig. 1 Schematic of 76.8 mm RDRE configurations: (a) heat-sink straight channel, (b) water-cooled straight channel, and (c) water-cooled constricted geometry.**

### B. Calorimetry Hardware

The calorimeter, as with the heat-sink outer body, is additively manufactured out of GRCop-42. The hardware consists of 18 total circumferential cooling channels, where water is supplied by three inlets with measurements taken from two channels grouped together, comprising nine total axial stations. Using this configuration, heat flux measurements are taken at nine axial locations spaced 0.1 mm apart starting from the injector face to the combustor exit (see. Fig. 2). Water is supplied to the cooling channels via three inlet manifolds. Each of these manifolds internally separates the flow into six channels that travel around the outer body circumferentially and recombine into three distinct outlet channels creating a total of three coolant inlets and nine coolant outlets. Internally, the cooling channels incorporate a parallelogram cross sectional profile where the the top of the internal channels are kept within 30° of vertical due to AM constraints [14]. The channels wrap circumferentially to the exit manifold 180° from the inlet,

six of which are staggered at 160° and 200° from the inlet position to provide appropriate clearance for diagnostics (Fig. 3(b)-(d)).

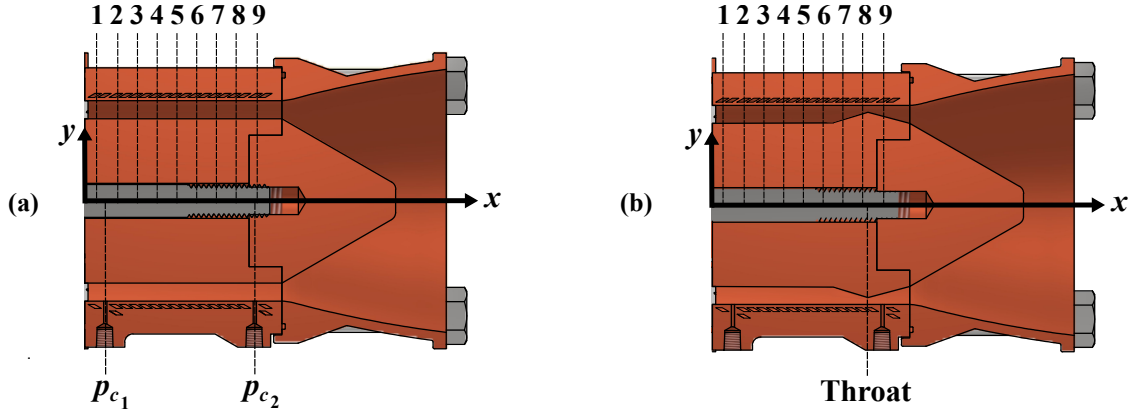



**Fig. 2 Schematics of 76.8 mm RDRE with water-cooled calorimetry outer body utilizing the (a) straight center body and (b) constricted center body.**

To allow for the measurement of the chamber pressure through the outer body, the internal geometry is such that the cooling channels are locally raised around capillary tube attenuated pressure (CTAP) sensor ports at axial locations $x/L = 0.10$ and 0.86 (Fig. 2(a)). The CTAP port is a straight 0.83 mm teardrop hole normal to the surface of the inner wall. To provide an isolated measurement of the static pressure, it is required that the CTAP holes are normal to the axial flow path to avoid introducing error by angling the CTAP hole [15]. During the calorimetry tests, only $p_{c_1}$ is measured to provide a chamber pressure measurement at $x/L = 0.10$.

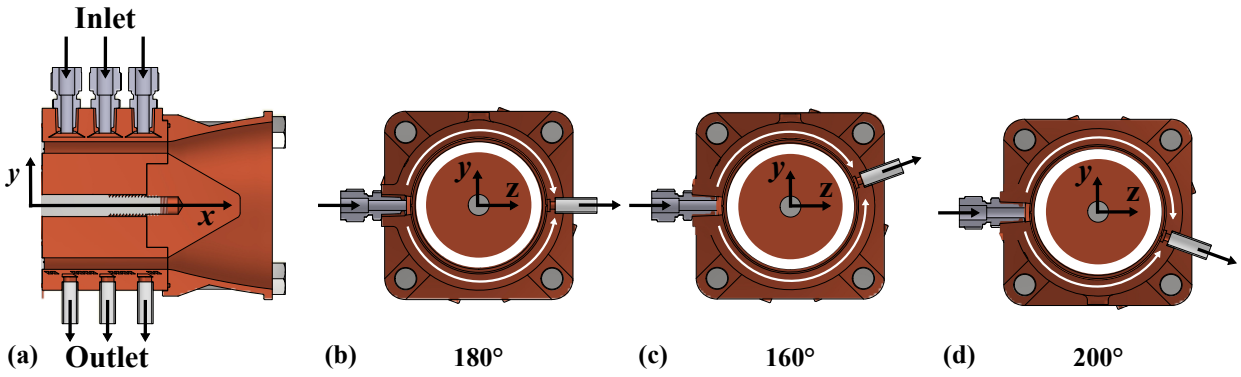



**Fig. 3 Schematics of the (a) coolant flow path, and outlet orientation of (b) 180°, (c) 160°, and (d) 200°.**

### C. Coolant Channel Geometry Sizing

To appropriately design the cooling channels, several factors are considered following the methodology laid out by Hernandez-McCloskey et al. [16]. First, it is critical to know the maximum coolant flow rate for the facility. In this study, a 12.4 MPa, 227 liter coolant tank is used to supply deionized water through the RDRE's cooling channels. At the maximum working system pressure of 12.4 MPa, the theoretical facility flow rate is 120 kg/s. However, the coolant delivery rate is ultimately limited by the flow resistance of the hardware's internal channels and the pressure loss through the coolant supply plumbing. Therefore, the channel resistances and the downstream flow metering orifices are also calibrated through a catch-and-weigh process, with the corresponding discharge coefficient, $C_d$, for each channel presented in Table 1. Overall, the hardware channels have an average discharge coefficient of $C_d = 0.113$; roughness of the internal channels and the constricted area through the channels are attributed as the major flow resistance factors contributing to the low $C_d$ values. Taking into account the flow losses through the calorimeter hardware, the maximum total coolant flow rate for this hardware becomes 13.5 kg/s.

**Table 1 Calibrated Discharge Coefficients**

| Station | 1 | 2 | 3 | 4 | 5 | 6 | 7 | 8 | 9 |
|---|---|---|---|---|---|---|---|---|---|
| **Axial Location, *x/L*** | 0.058 | 0.166 | 0.266 | 0.366 | 0.466 | 0.566 | 0.666 | 0.766 | 0.866 |
| **Channel $C_d$** | 0.111 | 0.089 | 0.111 | 0.113 | 0.123 | 0.107 | 0.124 | 0.124 | 0.111 |
| **Orifice $C_d$** | 0.917 | 0.673 | 0.792 | 0.808 | 0.807 | 0.655 | 0.778 | 0.769 | 0.741 |

The required coolant flow rate is dependent upon the amount of heat flux originating from combustion of the propellants to the combustion chamber wall, as well as the internal geometry of the cooling channels. In order to perform the initial coolant flow rate analysis, wall conduction-based heat flux measurements for a similarly sized 76.2 mm OD design taken by Micka et al. [4] for gaseous methane-oxygen are used. This work reports a maximum heat flux closest to the injector face of 25 MW/m$^2$ for a total propellant mass flow of $\dot{m}$ = 0.34 kg/s at an equivalence ratio ($\phi$) of 1.15. Additionally, for a larger engine (OD = 100 mm) used in Aliakbara et al. [10] shows heat flux approaching 8.25 MW/m$^2$ for a total propellant mass flow of $\dot{m}$ = 0.5 kg/s at an equivalence ratio of $\phi$ = 1.2. Assuming an equivalent heat transfer for a 76.8 mm combustor provides an estimated heat flux of 5 MW/m$^2$. These heat fluxes are used as bounds to determine the required coolant mass flow rate for the 76.8 mm calorimetry hardware implemented in this study, as the present work has a nominal operating condition of $\dot{m}$ = 0.33 kg/s and $\phi$ = 1.1.

The total heat flux is assumed to be evenly distributed along the combustor outer wall. The heat transfer rate to the combustor wall, $\dot{q}$, is then determined by multiplying the heat flux by the geometry's outer wall surface area as

$$\dot{q} = \dot{q}'' A_{\text{outer}}. \tag{1}$$

To minimize the uncertainty of the calorimetry measurements, the coolant needs to be kept below its saturation temperature. This is done to prevent nucleate boiling from occurring within the coolant channels, which can locally alter the heat transfer coefficient, $h_c$, from the wall to the coolant. This is undesirable for calorimetry applications as the nucleate boiling causes locally increased heat transfer into the coolant, leading to high uncertainty heat flux measurements. To avoid this, an initial coolant exit temperature target of $T_{\text{out}}$ = 600 K is taken as the saturation temperature of the coolant (i.e., deionized water) at the working pressure, $p$ = 12.4 MPa. The difference between ambient temperature ($T_{\text{in}}$ = 298 K) and this outlet temperature is used as the estimated target temperature rise across the hardware. Combining the initial temperature drop through the cooling channels and the experimentally determined value of the heat transfer rate, the mass flow required is given by

$$\dot{m} = \frac{\dot{q}}{\bar{c}(T_{\text{out}} - T_{\text{in}})}, \tag{2}$$

where $T_{\text{in}}$ and $T_{\text{out}}$ are the coolant inlet and exit temperatures respectively, $\dot{m}$ is the coolant mass flow rate, and $\bar{c}$ is the average coolant specific heat capacity.

Next, the total cross-sectional area of the cooling channels, $A_{\text{cool}}$, is sized to determine the flow velocity associated with the required coolant mass flow rate. Kolb et al. [17] showed the limiting diameter for powder removal of a straight internal channel with a circular cross section to be 0.5 mm. Due to the long-curved channels of this calorimeter, an increased cross-sectional area is chosen to ensure powder removal. With fixed channel dimensions, the coolant channel velocity $v_{\text{cool}}$ is found to be 21 m/s through mass conservation assuming steady operation. The liquid film coefficient for flow in pipes, $h_c$, is used to model heat transfer in the cooling channels [18] and is determined using

$$h_c = 0.023\bar{c}\frac{\dot{m}}{A_{\text{cool}}}\left(\frac{D_h v_{\text{cool}}\rho}{\mu}\right)^{-0.2}\left(\frac{\mu\bar{c}}{\kappa}\right)^{-\frac{2}{3}}, \tag{3}$$

where $D_h$ is the hydraulic diameter, $\rho$ is the coolant density, $\kappa$ is the coolant thermal conductivity, and $\mu$ is the coolant dynamic viscosity [19]. This parameter is the heat transfer coefficient required to achieve the target temperature rise across the hardware.

Once the coolant side heat transfer coefficient is known, the heat transfer coefficient required by Newton's law of cooling ($h_{c,\text{req}}$) is determined using the anticipated local heat flux as

$$h_{c,\text{req}} = \frac{\dot{q}}{(T_{\text{bulk}} - T_{\text{wall}})}, \tag{4}$$

where the coolant channel bulk temperature is assumed to be the outlet temperature ($T_{\text{bulk}} = T_{\text{out}}$) and the hot wall temperature is assumed to be the coolant saturation temperature. To ensure that the hot chamber wall is sufficiently cooled, $h_{\text{c}}$ must be greater than $h_{\text{c,req}}$. To satisfy this condition, the target temperature drop of coolant in the channels ($\Delta T$) is decreased by lowering $T_{\text{out}}$ and iterating until $h_c > h_{\text{c,req}}$.

Overall, the flow rate necessary to cool the higher heat flux seen in Micka et al. of 25 MW/m$^2$ is determined to be 4.5 kg/s, while the necessary flow rate to cool 9 MW/m$^2$ is found to be 1.36 kg/s. Both of these required flow rates fall within the flow rate capability of the facility. Therefore, this is a conservative required coolant flow rate estimation that is consistent with the experimental coolant mass flow rate.

## IV. Experimental Methods

For the calorimetry testing, the engine is mounted to a 22 kN thrust stand where propellant is supplied to the engine by compressed gas cylinders (four fuel and six oxidizer) and is regulated using dome-loaded pressure regulators. The propellants used in this study are gaseous methane ($GCH_4$) and oxygen ($GO_2$), with their mass flow rate measured using critical flow orifices [20], where pressure and temperature measurements are taken immediately upstream with static pressure transducers and T-type thermocouples, respectively. In the injector manifold, oxygen and fuel plenum pressures are measured using static pressure transducers and K-type thermocouples. All diagnostics in the experimental setup are sampled with a National Instruments-based data acquisition system at 1 kHz for all pressures and 90 Hz for all temperatures.

The cooling water is provided by a pressurized tank utilizing gaseous nitrogen ($GN_2$) for head pressure and is set to 2 kg/s for each test. Stainless steel tubing (25.4 mm) runs from the tank to a manifold block that splits the flow of coolant into the three 9.53 mm tubes that provide water to the calorimeter inlets. Inlet pressure and temperature are measured upstream of the manifold block. Coolant outlet pressure and temperature are taken 10 mm downstream of the hardware for each of the nine outlets static pressure transducers and T-Type thermocouples. The coolant mass flow rate is measured on a per outlet basis using nine calibrated 4.37 mm orifices immediately downstream of the outlet pressure and temperature measurements (Fig. 4(b)).

Wave dynamics are identified using high-speed visible luminescent imaging of the detonations provided by a Phantom TMX 5010 and a 200 mm lens (Nikon AF Micro-NIKKOR 200mm f/4.0D IF-ED) directed down the annulus of the engine via a mirror positioned in line with the exit of the combustor. High-speed imaging is captured at 200 kfps at a resolution of 256x128 px.




**Fig. 4 Images of (a) RDRE hot-fire and (b) hardware with instrumentation on thrust stand.**

### A. Heat Flux Determination

To determine the average heat flux distribution along the outer wall of the combustion chamber, the mass flow rate through the cooling channel is first determined. Pressure and temperature at each outlet is used to determine the mass flow rate associated with each of the cooling channels as

$$\dot{m}_n = \frac{\pi}{4} C_{\text{d}_n} A_n \sqrt{\frac{2\rho_n (p_{1_n} - p_2)}{1 - \beta_n^4}}, \tag{5}$$

where $\beta_n = D_{2_n}/D_1$, $D_1$ is the upstream tube diameter, $D_{2_n}$ is the orifice throat diameter, $A_n$ is the orifice throat area, $C_{d_n}$ is the discharge coefficient of the respective cooling channel from Table 1, $p_{1_n}$ is the coolant pressure immediately upstream of the orifice, $p_2$ is the atmospheric pressure directly downstream of the outlet orifice, and density, $\rho_n$, is the density upstream of the orifice for a given cooling channel $n$. This density is determined by using an open-source thermophysical property library [21], obtaining density at the outlet temperature and pressure. This mass flow rate is then used to determine the average heat that is convected out of the channels by the cooling water. Using this mass flow rate, the average convected heat flux can be written as

$$\dot{q}'' = \dot{m}\bar{c}(T_{\text{out}} - T_{\text{in}})/A_{\text{hot}}, \tag{6}$$

where the specific heat capacity $\bar{c}$ is taken at the coolant channel average temperature. Also, $T_{\text{in}}$ is the coolant temperature taken immediately upstream of the hardware and $T_{\text{out}}$ is the coolant temperature taken immediately downstream of the hardware. Here, $A_{\text{hot}}$ is taken to be the hot side are of the internal cooling channel.

Through the water flow calibration, the internal geometry of the AM channels exhibited adverse effects on the distribution of coolant mass flow through the channels. Particularly, the cooling channels in line with the inlet tubing (stations 2, 5, and 7) provide around twice as much coolant mass flow than the other channels. This large variation in mass flow rates results in the adiabatic assumption for the hot wall not being applicable, as this approach neglects the fact that heat is transferred between channels.

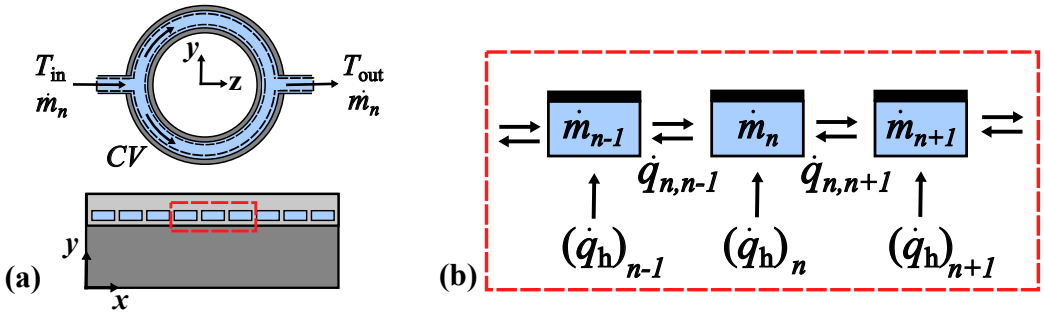



**Fig. 5 Schematic of (a) channel geometry control volume and (b) heat transfer model for determining chamber heat flux.**

To better represent the heat flux for this system, $\dot{q}$" is calculated by using an approach that accounts for heat being conducted between channels. In this model, the channel wall facing the ambient environment is taken to be adiabatic, where $(\dot{q}_{\text{h}})_{n-1}$ , $(\dot{q}_{\text{h}})_n$, and $(\dot{q}_{\text{h}})_{n+1}$ represent the heat flux distribution along the combustor wall (see Fig. 5(b)). Inter-channel heat transfer is then represented via conduction through the wall separating each of the channels. For a given channel, $n$, the net heat flux into the cooling channel is

$$(\dot{q}_{\text{tot}})_n = \dot{q}_{n,n-1} + (\dot{q}_{\text{h}})_n + \dot{q}_{n,n+1}, \tag{7}$$

where $(\dot{q}_{\text{h}})_n$ is the heat transfer rate from the hot wall of the combustion chamber, and $\dot{q}_{n,n+1}$ and $\dot{q}_{n,n-1}$ are the rates of heat transferred by the adjacent channels to the left and right, respectively. Rearranging Eq. (7) to solve for $(\dot{q}_{\text{h}})_n$, the heat transferred to the combustor wall becomes

$$(\dot{q}_{\text{h}})_n = \dot{m}_n\bar{c}\Delta T_n - \kappa A_{\text{side}}\Delta T_{n,n-1}/d - \kappa A_{\text{side}}\Delta T_{n,n+1}/d, \tag{8}$$

where $\dot{m}$ is the mass flow rate calculated using Eq. (6), $\kappa$ is the thermal conductivity of GRCop-42 [19], $\Delta T_n$ is the temperature difference between the inlet and the outlet of a channel $n$, and $\Delta T_{n,n+1}$ is the difference in temperature between a given channel and its adjacent channels. $A_{\text{side}}$ is the side wall area of the cooling channel, and $d$ is the distance between adjacent cooling channels. This result is then divided by the hot wall area of the cooling channel, $A_{\text{hot}}$, to get the heat flux along the hot side of the cooling channels taken to be the heat flux along the combustor wall. This model is implemented to determine heat flux for axial stations $2-8$. Also, as the wall temperatures adjacent to the first and last station are not known, the heat flux is not reported for those stations.

## V. Experimental Results

A mass flux sensitivity study is carried out by increasing the total propellant mass flux for a fixed equivalence ratio of $\phi = 1.1$ varying the propellant mass flux from $\psi = 103 - 310$ kg/m$^2$-s (Fig. 6(a)). The axial heat flux distribution is determined for a total of ten cases. Six set conditions are investigated with the water-cooled straight channel configuration with the total mass flux ranging from $\psi = 103 - 310$ kg/m$^2$-s. Four equivalent conditions are tested from $\psi = 103 - 240$ kg/m$^2$-s with the water-cooled constricted geometry configuration. A burn time of $t_b = 3.5$ s is considered for the water-cooled straight channel cases and a burn time of $t_b = 4.5$ s is considered for the water-cooled constricted geometry tests. Increased burn time allows for the engine hardware to reach thermal steady-state, and is evaluated using the outlet coolant temperatures of the different axial stations. Data from the steady-state portion for each test is averaged over a 200 ms window that is used for the heat flux determination. As an example, during the $\psi = 241$ kg/m$^2$-s straight center body case, stations $2 - 8$ reach thermal steady-state after $t = 2.5$ s (Fig. 6(b)), while stations 1 and 9 do not fully reach thermal steady-state within the duration of the test as they lack an adjacent cooling channel to one side.

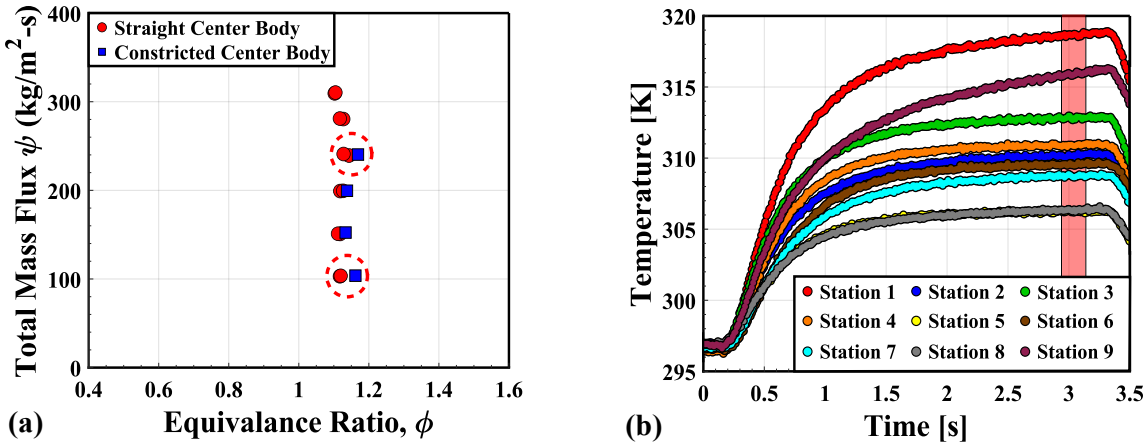



**Fig. 6 (a) Operational map and (b) outlet temperature response for $\psi = 241$ kg/m$^2$-s, $\phi = 1.1$ test.**

The low mass flux case at $\psi = 103$ kg/m$^2$-s (Fig. 7(a)), and the high mass flux case at $\psi = 240$ kg/m$^2$-s (Fig. 7(b)), demonstrate an increase in heat flux loading as a function of total mass flow rate. For the $\psi = 103$ kg/m$^2$-s case, heat flux ranges from $5 - 8$ MW/m$^2$ for the straight center body case and $7.5 - 13$ MW/m$^2$ for the constricted center body case. In addition, there is increased spatial heat flux from $x/L = 0.2 - 0.6$, most likely corresponding to the axial location of the detonation zone, with a maximum heat flux of 7.7 MW/m$^2$ for the low mass flux case. Over the same axial region, the constricted center body case experiences increased heat flux with a local maximum of 10.5 MW/m$^2$. From $x/L = 0.55 - 0.80$, heat flux increases to 13 MW/m$^2$, corresponding to the axial location of the throat for the constricted center body case. Similar trends are observed in the high mass flux case at $\psi = 240$ kg/m$^2$-s, where the heat flux ranges from $9 - 11.5$ MW/m$^2$ for the straight configuration and $9 - 17$ MW/m$^2$ with the constricted geometry. The heat flux reaches a maximum of 11.5 MW/m$^2$ at $x/L = 0.27$ for the straight channel, a comparable trend to the low flux case. However, the detonation region appears to be pushed further downstream axially ($x/L = 0.35 - 0.60$) for the $\psi = 240$ kg/m$^2$-s case due to an increased propellant mass flow rate, reaching a local maximum of 13.25 MW/m$^2$ at $x/L = 0.47$.

As expected, the straight center body configuration results in lower heat flux overall compared to the constricted center body configuration for comparable propellant mass flux in the straight chamber geometry, ranging from $5.75 - 11.25$ MW/m$^2$ (Fig. 8(a)). Additionally, the heat flux increases with mass flux such that the peak heat flux for the $\psi = 310$ kg/m$^2$-s case is 46% greater than the maximum heat flux of the $\psi = 103$ kg/m$^2$-s case. When considering the axial heat flux distribution profiles, there is an area of consistent increased heat flux from $x/L = 0.17 - 0.47$ for each straight center body mass flux condition. Downstream of this region the heat flux then decreases with axial length after $x/L = 0.47$. Finally, the heat flux at $x/L = 0.37$ for the straight center body is approximately 28% lower than the average heat flux of the constricted center body at the same location.

Overall, the constricted center body geometry results in higher maximum heat flux loadings for all cases tested (Fig. 8(b)). Across the four conditions, the heat flux varied from $7.5 - 17$ MW/m$^2$. For the $\psi = 240$ kg/m$^2$-s case, the maximum heat flux is 32% higher than the $\psi = 103$ kg/m$^2$-s case. Upon observing the spatial heat flux distribution,

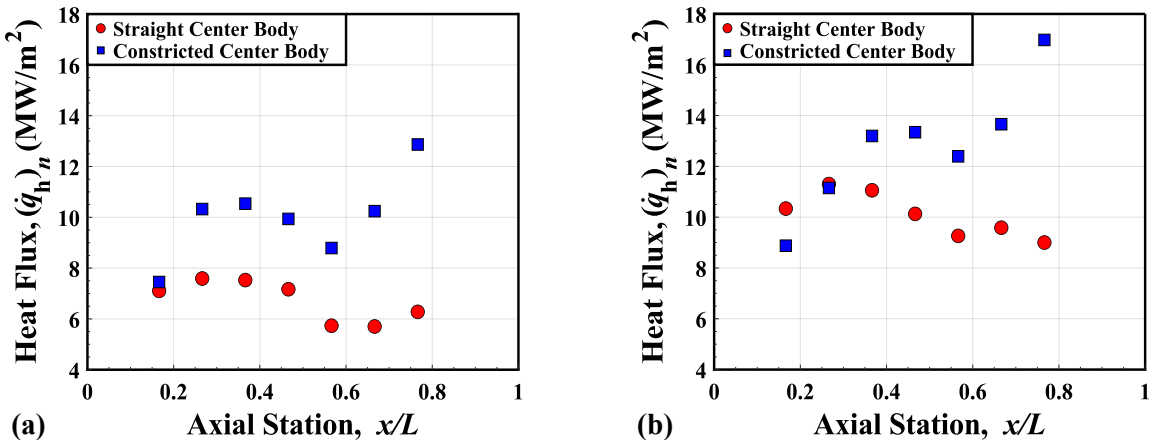



**Fig. 7 Axial heat flux distribution for (a) $\phi$ = 1.1 and $\psi$ = 103 kg/m$^2$-s and (b) $\phi$ = 1.1 and $\psi$ = 240 kg/m$^2$-s for both straight and constricted center bodies.**

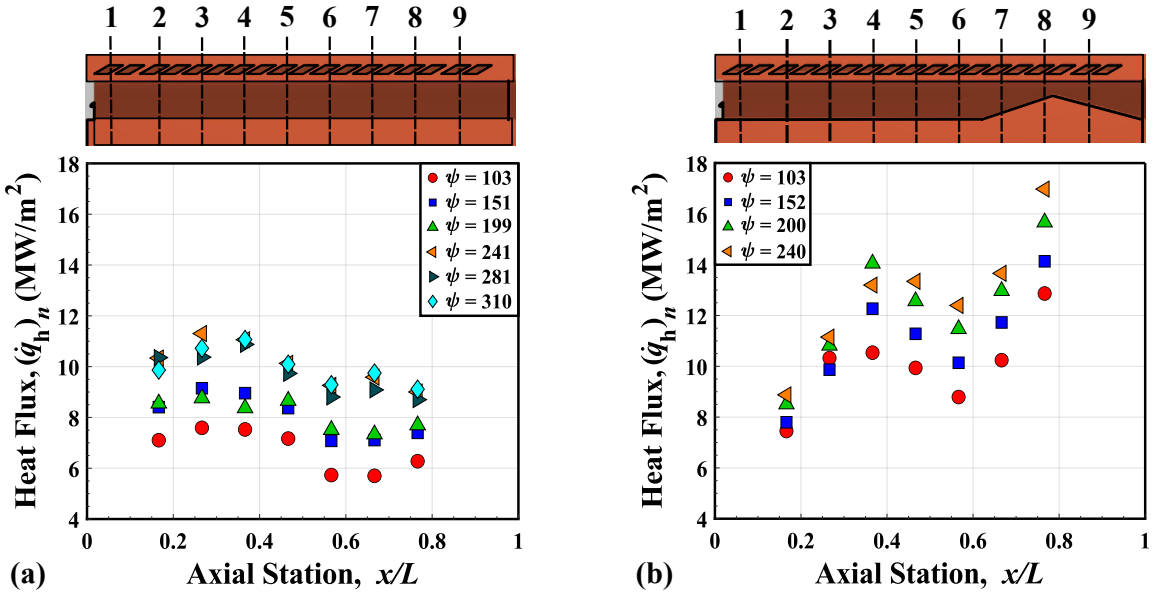



**Fig. 8 Axial heat flux distributions for (a) straight center body tests and (b) constricted center body tests.**

there is a sharp increase in $(\dot{q}_h)_n$ from $x/L = 0.17 - 0.37$, followed by a decrease from $x/L = 0.37 - 0.57$ for all mass flux conditions. There is then a rapid increase in heat flux as the geometry constricts beginning at $x/L = 0.57$ and ending at a maximum heat flux of 17 MW/m$^2$ at the throat ($x/L = 0.77$). For the constricted geometry cases, there is less variation between heat flux loads near the injection plane, where the heat flux variation between different mass flux conditions from $x/L = 0.17 - 0.27$ is nearly twice as much as the variation in heat flux after $x/L = 0.37$ for each condition. This is consistent with results seen by Micka et al. [4], demonstrating a difference in heat flux scaling near the injector compared to the flow expansion further downstream.

Apart from the general heat flux trends observed for the straight and constricted geometries for varying mass flux conditions, other testing was performed to evaluate the influence of operating mode on heat flux levels. In one $t_b$ = 4.5 s test at $\phi$ = 1.1, $\psi$ = 279 kg/m$^2$, the operating mode dynamics are shown to influence the heat flux experienced by the combustor. For this test, operating mode parameters were analyzed using an in-house python image processing code based on the work of Bennewitz et al. [22] to automatically extract wave mode, speed and mode frequency. For a total mass flux of $\psi$ = 279 kg/m$^2$-s, the station one outlet temperature appears to reach a steady-state temperature of $T_{out}$ = 320 K, however, there is a sudden increase in the slope of the temperature measurement occurring at $t$ = 3.2 s (see Fig. 9(a)). From the beginning of the test, a single counter-clockwise rotating wave is seen until $t$ = 3.2 s

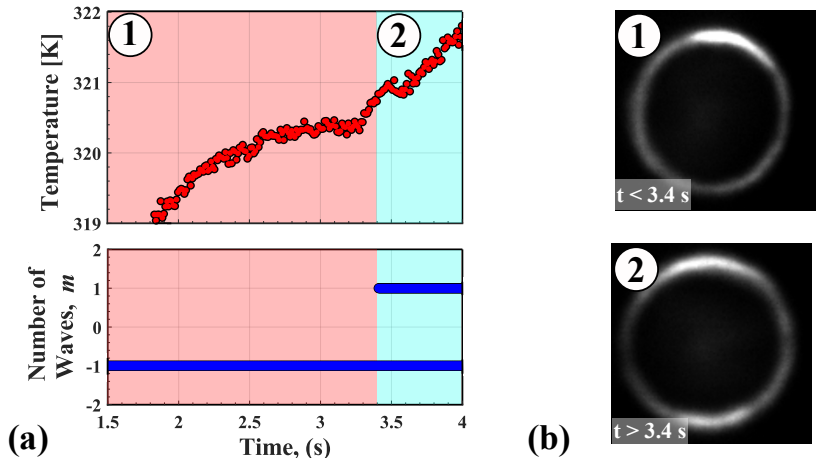



**Fig. 9 Constricted geometry test case at $\psi$ = 279 kg/m$^2$-s, exhibiting (a) temperature rise associated with change in wave mode and (b) accompanying high speed images of wave dynamics.**

when the observed wave mode begins to transition from a (1) one wave rotating mode to (2) one wave with single counter-propagating wave mode (Fig. 9(b)). During this transition period, from $t = 3.2 - 3.4$ s, a second wave traveling in the opposite begins to develop. At $t = 3.4$ s the wave dynamic fully transitions to a one wave rotating with one wave counter propagating mode. This closely corresponds with the sudden jump in coolant outlet temperature. This rise in temperature is observed across the first four stations ($x/L = 0.06 - 0.37$) most likely corresponding to the axial location of the detonation zone. However, this is not observed for stations further downstream than $x/L = 0.37$ implying the increase in heat flux due to an increase in wave number has a stronger influence closer to the injector than further downstream in the flow expansion section. This change in wave mode leads to increased heat flux to the chamber wall demonstrating that heat flux is not only dependent upon total mass flux, but also upon wave dynamics within the combustion chamber.

## VI. Conclusion

Experimentally measured heat flux data is presented for a 76.8 mm additively manufactured water-based calorimetry RDRE outer body operating with gaseous methane ($GCH_4$) and oxygen ($GO_2$). The hardware is tested with both a straight and constricted center body configuration at an equivalence ratio of $\phi = 1.1$ and total mass flux ranging from $\psi = 103 - 310$ kg/m$^2$-s. Average heat flux is determined to be between $5 - 12$ MW/m$^2$ for the straight center body tests and $6 - 18$ MW/m$^2$ for the constricted center body tests. Maximum heat flux occurs at $x/L = 0.27$ for the straight chamber tests and $x/L = 0.77$ for the constricted geometry cases; these two maximum heat flux regions correspond to the likely detonation zone and throat location for the straight and constricted geometries, respectively. These average heat flux measurements serve to increase the understanding of the thermal loads found in rotating detonation engines. The average heat flux measurements captured in this study help enhance the understanding for the heat flux loadings in detonation-based engines to ultimately help develop thermal management strategies enabling long duration operation.

## Acknowledgments

This work is sponsored by the National Aeronautics and Space Administration (NASA) Marshall Spaceflight Center (MSFC) under NASA CAN grant 80NSSC24M0062. The authors would like to thank Dr. David Lineberry and Tony Hall for their invaluable support with testing, as well as Raj Dave, Garrett Cobb, and the students of the Advanced Propulsion, Energy, and Combustion Science Laboratory.

## References

[1] Bennewitz, J. W., Burr, J. R., Bigler, B. R., Burke, R. F., Lemcherfi, A., Mundt, T., Rezzag, T., Plaehn, E. W., Sosa, J., Walters, I. V., Schumaker, S. A., Ahmed, K. A., Slabaugh, C. D., Knowlen, C., and Jr., W. A. H., "Experimental validation of rotating detonation

for rocket propulsion," *Scientific Reports*, Vol. 13, No. 1, 2023, p. 14204. https://doi.org/10.1038/s41598-023-40156-y, URL https://doi.org/10.1038/s41598-023-40156-y.

[2] Durkee, K. J., Dave, R. T., Maybee, M. A., Cobb, G. R., Burr, J. R., and Bennewitz, J. W., "Performance Measurements of a 25 mm Rotating Detonation Rocket Engine," 2024.

[3] Knowlen, C., Mundt, T., and Kurosaka, M., "Experimental results for 25-mm and 51-mm rotating detonation rocket engine combustors," *Shock Waves*, Vol. 33, No. 3, 2023, p. 237–252. https://doi.org/10.1007/s00193-023-01120-x, URL http://dx.doi.org/10.1007/s00193-023-01120-x.

[4] Micka, D. J., Daines, G., Sosa, J., Burke, R. F., Ahmed, K. A., Paulson, E., Bennewitz, J. W., Danczyk, S., and Hargus, W. A., "Heat Transfer Measurements in an Elevated Pressure RDRE Combustor," *AIAA Propulsion and Energy 2021 Forum*, American Institute of Aeronautics and Astronautics, 2021. https://doi.org/10.2514/6.2021-3685, URL http://dx.doi.org/10.2514/6.2021-3685.

[5] Bartz, D. R., "Survey of Relationships between Theory and Experiment for Convective Heat Transfer in Rocket Combustion Gases," *Advances in Rocket Propulsion*, 1968.

[6] Theuerkauf, S. W., Schauer, F., Anthony, R., and Hoke, J., "Experimental Characterization of High-Frequency Heat Flux in a Rotating Detonation Engine," *53rd AIAA Aerospace Sciences Meeting*, American Institute of Aeronautics and Astronautics, 2015. https://doi.org/10.2514/6.2015-1603, URL http://dx.doi.org/10.2514/6.2015-1603.

[7] Theuerkauf, S., King, P., Schauer, F., and Hoke, J., "Thermal Management for a Modular Rotating Detonation Engine," *51st AIAA Aerospace Sciences Meeting including the New Horizons Forum and Aerospace Exposition*, American Institute of Aeronautics and Astronautics, 2013. https://doi.org/10.2514/6.2013-1176, URL http://dx.doi.org/10.2514/6.2013-1176.

[8] Hernandez-McCloskey, J., Pineda, D. I., Bennewitz, J. W., Bigler, B. R., Burr, J. R., Danczyk, S. A., Paulson, E. J., and Hargus, W. A., "Design and analysis of an additively manufactured rotating detonation rocket engine chamber for calorimetry and thermal management assessment," *AIAA SCITECH 2023 Forum*, American Institute of Aeronautics and Astronautics, 2023. https://doi.org/10.2514/6.2023-0355, URL http://dx.doi.org/10.2514/6.2023-0355.

[9] Smallwood, J. S., and Heister, S. D., "Thermal and structural characterization of A rotating detonation rocket engine," *AIAA SCITECH 2024 Forum*, American Institute of Aeronautics and Astronautics, 2024. https://doi.org/10.2514/6.2024-0816, URL http://dx.doi.org/10.2514/6.2024-0816.

[10] R. Aliakbari, N. M.-S. A. P. M. W. N. P., Q. Michalski, "Heat Flux Measurements of a Methane-Oxygen Rotating Detonation Rocket Engine," *12th International Workshop on Detonation Propulsion*, 2022.

[11] Teasley, T. W., Fedotowsky, T. M., Gradl, P. R., Austin, B. L., and Heister, S. D., "Current State of NASA Continuously Rotating Detonation Cycle Engine Development," *AIAA SCITECH 2023 Forum*, American Institute of Aeronautics and Astronautics, 2023. https://doi.org/10.2514/6.2023-1873, URL http://dx.doi.org/10.2514/6.2023-1873.

[12] Cobb, D. K. B. J.-B. J., G., "Power Cycle Analysis in Actively Cooled Rotating Detonation Rocket Engines," *AIAA Scitech 2025 Forum (in Preperation)*, American Institute of Aeronautics and Astronautics, 2025.

[13] Burr, J. R., and Paulson, E., "Thermodynamic Performance Results for Rotating Detonation Rocket Engine with Distributed Heat Addition using Cantera," *AIAA Propulsion and Energy 2021 Forum*, American Institute of Aeronautics and Astronautics, 2021. https://doi.org/10.2514/6.2021-3682, URL http://dx.doi.org/10.2514/6.2021-3682.

[14] *Metal Additive Manufacturing for Propulsion Applications*, American Institute of Aeronautics and Astronautics, Inc., 2022. https://doi.org/10.2514/4.106279, URL http://dx.doi.org/10.2514/4.106279.

[15] Jr, R. E. R., "An investigation of the influence of orifice geometry on static pressure measurements," 1949.

[16] Hernandez-McCloskey, T. T. P.-D. R. S. A. P. D. I., J., "Calorimeter Heat Flux Trends in NASA's Subscale Rotating Detonation Rocket Engine," *AIAA Scitech 2025 Forum (in Preperation*, American Institute of Aeronautics and Astronautics, 2020.

[17] Kolb, T., Mahr, A., Huber, F., Tremel, J., and Schmidt, M., "Qualification of channels produced by laser powder bed fusion: Analysis of cleaning methods, flow rate and melt pool monitoring data," *Additive Manufacturing*, Vol. 25, 2019, p. 430–436. https://doi.org/10.1016/j.addma.2018.11.026, URL http://dx.doi.org/10.1016/j.addma.2018.11.026.

[18] Sutton, G., and Biblarz, O., *Rocket Propulsion Elements*, 2nd ed., John Wiley & Sons, Inc., 1956.

[19] Gradl, P. R., Protz, C. S., Cooper, K., Ellis, D., Evans, L. J., and Garcia, C., "GRCop-42 Development and Hot-fire Testing Using Additive Manufacturing Powder Bed Fusion for Channel-cooled Combustion Chambers," *AIAA Propulsion and Energy 2019 Forum*, American Institute of Aeronautics and Astronautics, 2019. https://doi.org/10.2514/6.2019-4228, URL http://dx.doi.org/10.2514/6.2019-4228.

[20] Rathsack, T., Bigler, B. R., Bennewitz, J. W., Danczyk, S. A., and Hargus, W. A., "Laboratory Flow Measurement in Rotating Detonation Rocket Engines," *AIAA Scitech 2020 Forum*, American Institute of Aeronautics and Astronautics, Orlando, FL, 2020. https://doi.org/10.2514/6.2020-0194, URL https://arc.aiaa.org/doi/10.2514/6.2020-0194.

[21] Bell, I. H., Wronski, J., Quoilin, S., and Lemort, V., "Pure and Pseudo-pure Fluid Thermophysical Property Evaluation and the Open-Source Thermophysical Property Library CoolProp," *Industrial & Engineering Chemistry Research*, Vol. 53, No. 6, 2014, pp. 2498–2508. https://doi.org/10.1021/ie4033999, URL http://pubs.acs.org/doi/abs/10.1021/ie4033999.

[22] Bennewitz, J. W., Bigler, B. R., Schumaker, S. A., and Hargus, J., W. A., "Automated image processing method to quantify rotating detonation wave behavior," *Review of Scientific Instruments*, Vol. 90, No. 6, 2019, p. 065106. https://doi.org/10.1063/1.5067256, URL https://doi.org/10.1063/1.5067256.